Quantifying Entrainment and Degassing of Bubbles by Free-Surface Turbulence for Ship Wake Applications

Declan B. Gaylo[1], Kelli Hendrickson[2,1], Dick K.P. Yue[1]
([1]Massachusetts Institute of Technology, USA, [2]University of North Carolina at Chapel Hill, USA)

ABSTRACT

The bubbly wake is a highly observable feature that persists far behind a vessel. Predicting the bubble population created by the air-entraining free surface turbulence (FST) in the near-wake region of the bubbly wake remains a challenge in computational ship hydrodynamics. Entrainment and degassing are the two mechanisms that determine the volume of entrained air; however, measuring instantaneous bubble populations only elucidates their net effect. Eulerian label advection (Gaylo *et al.*, 2022) provides accurate and robust tracking of every bubble in a simulation, enabling the first separate measurement of entrainment and degassing. Using ELA with ensemble direct numerical simulations of a canonical shear-flow FST at large Froude numbers, we elucidate the statistics of entrainment and degassing. To enable comparison to general FST flows, we report a second Froude number based on the turbulence in the near-surface region. For entrainment, we confirm that the size distribution follows $I(a) \propto a^{-10/3}$ predicted by Yu *et al.* (2020). Quantifying the volume flow rate of degassing relative to entrainment, we show that degassing significantly modifies the total entrained volume in FST, independent of large Fr^2. For degassing, we consider a bubble radius dependent degassing rate $\lambda(a)$ (units $[1/T]$). We elucidate two distinct degassing regimes, separated by the critical radius where turbulent velocity u_{rms} equals a bubble terminal rise velocity. This highlights the importance of both buoyant rise and turbulent advection in degassing models.

INTRODUCTION

In the flow around a vessel, strong turbulence in the water near the free surface leads to entrainment of air. This entrained air forms a cloud of bubbles referred to as the bubbly wake, which persists miles behind the vessel (Trevorrow *et al.*, 1994) and has distinct and highly observable acoustic and surface features (NDRC, 1946). Thus, understanding the extent of the bubbly wake as well as the size distribution of the bubble population within it is important to the design and operation of naval vessels.

The bubbly wake can be split into two regions: the near wake region where strong turbulence entrains a significant volume of air and fragments large bubbles into smaller bubbles; and the far wake region where the flow is more quiescent and bubbles slowly rise to the surface and degas as the air within them also dissolves into the water. While the far wake is a much larger region than the near wake, a current challenge in computational ship hydrodynamics is that accurate prediction of the far wake requires the total volume, spatial distribution, and size distribution of the bubble population created by entrainment and other physical mechanisms in the near wake. As fully resolved (both turbulent scales and bubble scales) simulation of the near wake is not possible with existing computational resources (Castro *et al.*, 2016), models are needed to describe these physical mechanisms. To this end, direct numerical simulation (DNS) of smaller-scale air-entraining free-surface turbulence (FST) provides physical insights and quantitative measurements to inform development of the models necessary for accurate prediction of the bubbly flow in the near wake.

This work uses DNS of air-entraining FST to study entrainment and degassing, including their interactions and relative strengths, in the near wake. Because dissolution of air into the water generally occurs on timescales much larger than those relevant to the near wake, the balance between entrainment and degassing determines the total volume of entrained air. While degassing has often been studied in the absence of free-surface entrainment (relevant to the far wake) (Thorpe, 1982; Ruth *et al.*, 2021), little is known about its effect when in combination with active entrainment, as in the near wake. Practically, measuring entrainment and degassing separately is a challenge, and previous studies only measure the net effect of the two. For example, Yu *et al.* (2020), while studying air entrainment in a canonical shear-flow FST, assumed that degassing was negligible so that they could use the change in total entrained volume to infer the physics of entrainment. However, with the computational tools available at the time, they could not evaluate this assumption.

Through ELA, we provide the first separate measurements of entrainment and degassing in a

near-wake turbulent free surface flow. We revisit the canonical shear-flow FST studied by Yu *et al.* (2020), but now with Eulerian label advection (ELA) (Gaylo *et al.*, 2022) to robustly track the evolution of bubbles during the simulation. With this new tool, we are able to identify individual entrainment and degassing events and then extract their statistics. For shear-flow FST, we first examine turbulence statistics near the free surface to provide a turbulence-based Froude number applicable to general FST. Looking at entrainment statistics, we verify that entrainment follows the size distribution predicted mechanistically by Yu *et al.* (2020). Comparing the volume flux due to entrainment to that due to degassing, we find that degassing is not negligible and significantly effects the total entrained volume, and that the relative strength of degassing to entrainment is Froude invariant. Looking at degassing statistics, we find two distinct regimes for the dependence on degassing rate on bubble radius, which we explain by comparing turbulent advection to buoyant rise of bubbles.

DESCRIBING BUBBLE POPULATIONS

Bubble Size Distribution, $N(a)$

The population of bubbles within a flow can be described by a size distribution $N(a)$, where $N(a)\delta a$ gives the number of bubbles of effective[1] radius $a < a' < a+\delta a$ within a domain of interest. As opposed to resolving individual bubbles, a common approach for computational ship hydrodynamics is to model the stochastic evolution of $N(a)$ using a population-balance equation (Castro & Carrica, 2013),

$$\frac{\partial N}{\partial t} = \mathcal{S}_d + \mathcal{S}_f + \mathcal{S}_c + I - D \quad , \tag{1}$$

where the terms on the right correspond to the five physical mechanisms that act on the bubbles. Three mechanisms move air among bubble sizes:

- $\mathcal{S}_d$ – dissolution of air into the water,
- $\mathcal{S}_f$ – fragmentation of bubbles,
- $\mathcal{S}_c$ – coalescence of bubbles,

and two mechanisms move air across the free surface:

- I – injection of bubble through entrainment at the free surface,
- D – loss of bubbles through degassing at the free surface.

Here, $I(a,t)\delta a\delta t$ is the number of bubbles radius $a < a' < a+\delta a$ that are entrained over $t < t' < t+\delta t$ within domain of interest, and the definition for $D(a,t)$ is similar.

[1]Defined by the volume v of a bubble: $a = (3v/4\pi)^{1/3}$.

Table 1: Regimes of bubble rise velocity for different Re_b, as described by Park *et al.* (2017).

Regime	Re_b	W_t
Viscous	< 1	$\frac{ga^2}{3\nu}$
Inertial	$1 - 100$	$0.408\ g^{5/6}\nu^{-2/3}a^{3/2}$
Cap	> 100	$1.02\ g^{1/2}a^{1/2}$

In both breaking waves (Deane & Stokes, 2002) and entrainment by turbulence (Yu *et al.*, 2020) it is often observed that the bubble size distribution follows $N(a) \propto a^{-10/3}$ for large bubbles, specifically, larger than the Hinze scale such that fragmentation is unaffected by surface tension (Hinze, 1955). Garrett *et al.* (2000) showed that a fragmentation cascade, where large bubbles successively fragment into smaller bubbles, creates this $-10/3$ power law. Considering fragmentation and entrainment together, it can be shown analytically that, at equilibrium, this fragmentation cascade will dominate and $N(a) \propto a^{-10/3}$ will be observed if entrainment is weak, specifically, if $I(a) \propto a^{\gamma}$ where $\gamma \geq -4$ (Gaylo *et al.*, 2021). Gaylo *et al.* (2023) showed that this equilibrium fragmentation cascade is obtained very quickly in FST.

Looking at the entrainment size distribution $I(a)$, Yu *et al.* (2020) compare the energy available from turbulence and the energy necessary to create a bubble to predicted $I(a) \propto a^{-10/3}$ for large bubbles, here meaning large in terms of Bond number. However, because this predicted entrainment is weak ($-10/3 \geq -4$) and happens to line up with the fragmentation cascade equilibrium for $N(a)$, it is difficult to confirm the presence of this entrainment size distribution based on observations of $N(a)$ alone.

Degassing of a bubble happens when it rises to the free surface. For void fractions small enough that the local turbulence in the water is unaffected by the presences of air bubbles, we expect the movement of individual bubbles to be independent. The independence of individual bubbles implies that the degassing size distribution $D(a)$ must depend linearly on the bubble population size distribution $N(a)$. Based on this assumption, we can define a degassing rate $\lambda(a)$ (units $1/T$) given by

$$\lambda(a) \equiv \frac{D(a)}{N(a)} \quad , \tag{2}$$

which should be a function of turbulence and bubble radius, but independent of $N(a)$. Because degassing is the result of bubbles rising to the surface, models of degassing generally depend on the mean rise velocity of a bubble. For the simplest model, we have the terminal velocity of a bubble in quiescent flow, $W_t(a)$. As shown in table 1, this can be described by one of three regimes depending

on the bubble-rise Reynolds number (Park *et al.*, 2017),

$$Re_b \equiv \frac{2a\ W_t(a)}{\nu} \quad . \tag{3}$$

More detailed models are available for non-quiescent flows where mean rise velocity is effected by turbulence (Ruth *et al.*, 2021); however, degassing has not been studied in FST where entrainment is also present, as is the case in the near wake we are interested in modeling.

Total Entrained Volume, V

Related to the size distribution of bubbles described by $N(a)$, a simple scalar quantity is the total volume of entrained air,

$$V = \frac{4\pi}{3}\int_0^\infty N(a)a^3\,\mathrm{d}a \quad . \tag{4}$$

Fragmentation and coalescence do not cause any change in the total entrained volume, and dissolution is negligible for the large bubbles and short timescales relevant to the near wake, so the evolution of the total entrained volume is

$$\frac{\partial V}{\partial t} = Q_I - Q_D \quad , \tag{5}$$

where the entrainment flow rate is

$$Q_I = \frac{4\pi}{3}\int_0^\infty I(a)a^3\,\mathrm{d}a \quad , \tag{6a}$$

and the degassing flow rate is

$$Q_D = \frac{4\pi}{3}\int_0^\infty D(a)a^3\,\mathrm{d}a \quad . \tag{6b}$$

The size distribution $N(a)$ provides a detailed description of the bubble population, and the size of bubbles is certainly relevant to the evolution of the bubbly wake and its observable features. However, we find that total entrained volume, being a scalar quantity rather than a distribution, provides a useful metric to characterize the evolution of the bubbly wake, particularly in the near wake where we expect large $\partial V/\partial t$ driven by the presence of entrainment.

SIMULATION METHODOLOGY

We perform DNS of the two-phase, incompressible, three-dimensional Navier-Stokes equations on a uniform Cartesian grid using the conservative volume of fluid method (cVOF) (Weymouth & Yue, 2010). During the simulation, Eulerian label advection (ELA) tracks the volume of individual bubbles (Gaylo *et al.*, 2022). This provides a volume-based (conservative) description of the evolution of bubbles in the simulation, from which we can extract entrainment and degassing statistics.

Two-Phase DNS Solver

For immiscible fluids, a volume of fluid method is defined based on the color function,

$$c(\mathbf{x}) = \begin{cases} 1 & \text{if} \quad \mathbf{x} \in \text{air} \\ 0 & \text{if} \quad \mathbf{x} \in \text{water} \end{cases} \quad . \tag{7}$$

From this color function, density and viscosity are calculated

$$\rho = c\ \rho_a + (1-c)\ \rho_w \quad , \tag{8a}$$

$$\mu = c\ \mu_a + (1-c)\ \mu_w \quad . \tag{8b}$$

For air and sea water, we use $\rho_a/\rho_w = 0.00123$ and $\mu_a/\mu_w = 0.0159$. In the present study, we neglect surface tension, corresponding to Weber numbers $We \sim \infty$. For our DNS method, Yu *et al.* (2019) verify that neglecting surface tension accurately captures limiting $We \gg 1$.

For two-phase immiscible flow, we have three governing equations: volume conservation

$$\nabla \cdot \mathbf{u} = 0 \quad , \tag{9a}$$

momentum conservation

$$\frac{\partial \mathbf{u}}{\partial t} + \mathbf{u}\cdot\nabla\mathbf{u} = -\frac{1}{\rho}\nabla p + \frac{1}{\rho Re}\nabla\cdot(2\mu\mathbf{E}) - \frac{\hat{\mathbf{e}}_z}{Fr^2} \quad , \tag{9b}$$

where p is the pressure field and $\mathbf{E}$ is the rate-of-strain tensor $1/2(\nabla\mathbf{u} + \nabla\mathbf{u}^{\mathrm{T}})$, and phase conservation

$$\frac{\partial c}{\partial t} + \mathbf{u}\cdot\nabla c = 0 \quad . \tag{9c}$$

We discretize these equations using a staggered-grid finite-volume method with second-order central differences for the convective terms. An explicit second-order predictor-corrector method estimates the time integral in Eq. (9b). The pressure is determined from the continuity equation using the projection method, the resulting Poisson equation solved using GMRES, as implemented in *hypre* (Falgout *et al.*, 2006). Yu *et al.* (2019) provide the numerical verification of this approach with FST.

For the color function, the average value of $c(\mathbf{x})$ in the volume of computational cell defines the volume of fluid (VOF) field,

$$f_{ijk} \equiv \frac{1}{\Delta^3}\iiint_{\Omega_{ijk}} c(\mathbf{x})\mathrm{d}\mathbf{x} \quad . \tag{10}$$

To find $\Delta f = f^{k+1} - f^k$ to advance the VOF field in time from t^k to $t^{k+1} = t^k + \Delta t$, we use operator split advection to discretize Eq. (9c),

$$\Delta f = \frac{\Delta t}{\Delta x^3}\left(\Delta_d F_d + \tilde{c}\frac{\partial u_d}{\partial x_d}\Delta x^3\right) \quad \text{for} \quad d \in 1\ldots 3 \quad . \tag{11}$$

Specifically, we use the cVOF method (Weymouth & Yue, 2010), where the difference in flux between the two faces in a direction $\Delta_d F_d = F_{d+1/2} - F_{d-1/2}$ is calculated using a second-order geometric interface reconstruction, and the dilation term is calculated using $\tilde{c}$, a binary approximation of $c(\mathbf{x})$. As proven by Weymouth & Yue (2010), this explicit method conserves volume of air and water to machine precision.

Tracking Bubbles with ELA

Identifying entrainment and degassing requires robust tracking of (many) individual bubbles through time. cVOF provides the complete (numerical) evolution of the VOF field, specifying at any point in time where all the air is in the simulation. However, this is not sufficient for tracking, where we need to know where the air in each bubble came from. To obtain this, we use Eulerian label advection (ELA) (Gaylo *et al.*, 2022). Alternative post-processing-based tracking approaches seek the 'most likely' explanation for how bubbles evolved between two snapshots in time t^n and t^{n+1} separated by a snapshot interval T_s (generally much larger than the simulation time step Δt). With ELA, we introduce a label field at time t^n describing which bubble air is in, and through one-way coupling with Eq. (11), this label field is advected along with the air. Thus, at time t^{n+1}, we have an explicit description of how air volume (and by extension bubbles) evolved over the snapshot interval T_s. Below we provide an overview of ELA, and more details are available from Gaylo *et al.* (2023),

At t^n, we identify contiguous connected regions of air (i.e., bubbles) and assign each a unique label ℓ. This first step is, more generally, the process of connected-component labeling (CCL) (He *et al.*, 2017), and many connection criteria have been proposed. Here, we use normals-based informed component labeling method (ICL) (Hendrickson *et al.*, 2020). From the unique labels assigned by ICL, we can define a vector color function $\mathbf{c}^n(\mathbf{x}, t)$, where each component is given at $t = t^n$ by

$$c_\ell^n(\mathbf{x}, t^n) \equiv \begin{cases} 1 & \text{if} \quad \mathbf{x} \in \text{bubble } \ell \\ 0 & \text{else} \end{cases} \quad . \tag{12}$$

In effect, Eq. (12) splits the color function into a vector of many color functions, one for each bubble present at t^n. The same phase conservation equation applies for these split color functions,

$$\frac{\partial \mathbf{c}^n}{\partial t} + \mathbf{u} \cdot \nabla \mathbf{c}^n = 0 \quad . \tag{13}$$

Analogous to VOF, discretizing this split color function,

$$\mathbf{s}_{ijk}^n(t) \equiv \frac{1}{\Delta x^3} \iiint_{\Omega_{ijk}} \mathbf{c}^n(\mathbf{x}, t) \mathrm{d}\mathbf{x} \quad , \tag{14}$$

and advancing it in time using an operator split method

$$\Delta \mathbf{s}^n = \frac{\Delta t}{\Delta x^3} \left(\Delta_d \mathbf{F}_d + \tilde{\mathbf{c}} \frac{\partial u_d}{\partial x_d} \Delta x^3 \right) \text{ for } d \in 1 \ldots 3 \quad . \tag{15}$$

Gaylo *et al.* (2022) provide an efficient way to obtain the vector expressions $\Delta_d \mathbf{F}_d$ and $\tilde{\mathbf{c}}$ from the scalar terms $\Delta_d F_d$ and $\tilde{c}$ used by cVOF in Eq. (11), creating a one-way coupling between the VOF advection scheme and bubble tracking. Gaylo *et al.* (2022) prove that ELA gives a volume conservative to machine precision solution to Eq. (15).

Using ELA, we advance $\mathbf{c}^n(\mathbf{x}, t^n)$ (discretized as $\mathbf{s}^n$) in time to $\mathbf{c}^n(\mathbf{x}, t^{n+1})$. This means that for any air particle at time t^{n+1}, we know which bubble it was in at time t^n. When we run ICL again at t^{n+1}, we obtain a new set of bubbles, and (with Eq. (12)) a new vector color function $\mathbf{c}^{n+1}$. To express the evolution of bubbles between t^n and t^{n+1}, we can define a volume tracking matrix (VTM) $\mathbf{Q}^n$, where each element

$$q_{ij}^n \equiv \iiint_\forall c_j^n(\mathbf{x}, t^{n+1}) c_i^{n+1}(\mathbf{x}, t^{n+1}) \, \mathrm{d}\mathbf{x} \tag{16}$$

describes the volume of air that went from a bubble labeled j at time t^n to a bubble labeled i at time t^{n+1}. This VTM provides a robust volume-based description of bubble evolution, from which physical mechanisms can be identified.

Extracting Entrainment and Degassing Statistics

Fig. 1 shows an illustration of how entrainment and degassing can be extracted from a VTM. For ELA, the bulk region of air above the free surface, the sky, is also treated as a bubble. To simplify notation, suppose ICL always identifies this sky 'bubble' as label $\ell = 1$.

Consider a volume tracking matrix $\mathbf{Q}^n = q_{ij}^n$ of size $a \times b$. The relevant portions of the VTM for entrainment and degassing are the first column and the first row. The intersection q_{11} represents air volume that stays in the sky. The first row excluding q_{11},

$$\mathcal{V}_D^n \equiv \{ v \in \{ q_{1j}^n, \, j = 2 \ldots b \} \; : \; v > 0 \} \tag{17a}$$

gives the set of volumes of bubbles that were degassed between t^n and t^{n+1}. Similarly for the first column,

$$\mathcal{V}_I^n \equiv \{ v \in \{ q_{i1}^n, \, i = 2 \ldots a \} \; : \; v > 0 \} \tag{17b}$$

gives the set of volumes of bubbles that were entrained between t^n and t^{n+1}. This approach captures the correct entrained or degassed volume when only part of a bubble degases ($q_{13}^n < v_3^n$ in Fig. 1) or when only part of a bubble's volume comes from entrainment ($q_{31}^n < v_3^{n+1}$ in Fig. 1). We note that a bubble could be entrained after t^n and degas before t^{n+1}, which introduces some dependence on large T_s.

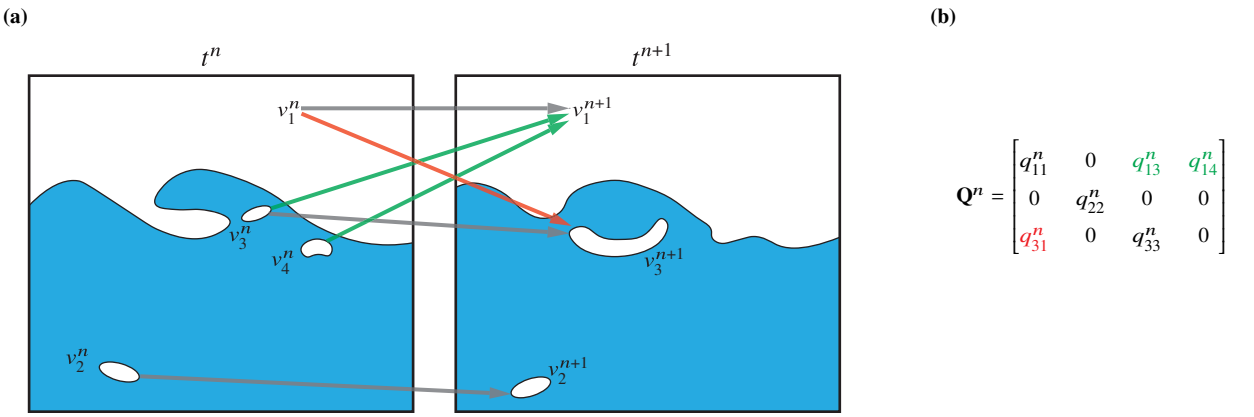

Figure 1: (a) Illustration of entrainment (red) and degassing (green); and (b) the associated volume tracking matrix $\mathbf{Q}^n = \{q_{ij}\}$ provided by ELA. At t^n, there are four contiguous regions of air (three bubbles and the 'sky') with volumes v_j^n and at $t^{n+1} = t^n + T_s$ there are three with volumes v_i^{n+1}. The degassed bubble volumes are $\mathcal{V}_D^n = \{q_{13}^n, q_{14}^n\}$ and the entrained bubble volumes are $\mathcal{V}_I^n = \{q_{31}^n\}$.

After converting from volume v to (effective) radius a, the distribution of $\mathcal{V}_D^n$ and $\mathcal{V}_I^n$ provide samples from the degassing size-distribution $D(a)T_s$ and the entrainment size-distribution $I(a)T_s$. In addition, summing $\mathcal{V}_D^n$ and $\mathcal{V}_I^n$ give samples of $Q_D T_s$ and $Q_I T_s$ respectively. From the set of bubbles identified by ICL, we also have a sample of $N(a)$, allowing us to calculate the degassing rate $\lambda(a)$. Using an ensemble of simulations and multiple snapshot intervals over the period of interest, we can obtain converged statistics.

SIMULATION SETUP

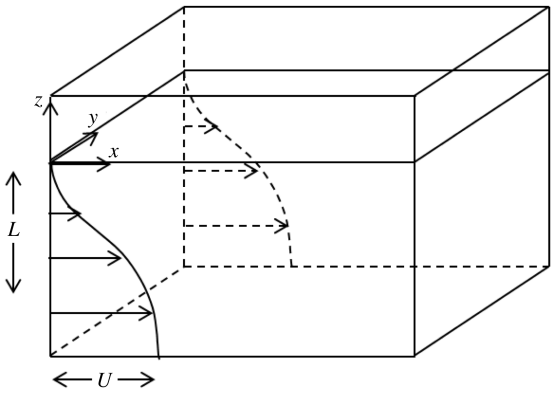

Figure 2: Shear flow initial condition with free surface at $z = 0$ and an initial shear profile given by Eq. (18). (Yu *et al.*, 2019)

We follow Yu *et al.* (2019) and consider the canonical problem of air entraining FST generated by the breakdown of a shear profile. This canonical problem captures features of the flow immediately behind a ventilated transom stern (Hendrickson *et al.*, 2019), and has been used to understand features of viscous ship wakes (Dimas & Triantafyllou, 1994). The initial condition sketched in Fig. 2). The shear profile,

$$u(z, t = 0)/U = 1 - 0.9988 \text{ sech}(0.88137\, z/L) \quad , \quad (18)$$

comes from the wake of a foil (Mattingly & Criminale, 1972). In the region of the strongest shear, we create an initial velocity perturbation (intensity $u_{\text{rms}}/U = 0.35$ and integral length scale $\ell_\infty/L = 0.08$) by filtering random white noise (Klein *et al.*, 2003). The rapid breakdown of this shear profile produces turbulence, including near the free surface.

The non-dimensional parameters for this shear-flow FST are the Froude number

$$Fr^2 = \frac{U^2}{gL} \quad , \quad (19)$$

and the Reynolds number

$$Re = \frac{UL}{\mu_w/\rho_w} \quad , \quad (20)$$

as well as the Weber number $We = U^2 L/(\sigma/\rho_w)$. From here on, we will normalize all values such that U and L are unity.

Following Yu *et al.* (2019), the domain size is $10.472 \times 10.472 \times 6$, with water initially in $z \in [-4, 0]$ and air $z \in [0, 2]$. For $Re = 1000$ studied here, a $384^2 \times 256$ grid ($\Delta x = 0.02$) resolves the Kolmogorov scale (see convergence study by Yu *et al.* (2019)). With surface tension neglected, the smallest bubbles that are considered resolved are radius $a_{\text{res}} = 1.5\Delta x$.

In this work we consider a range of Fr^2, as shown in table 2. For each Fr^2, the simulation is repeated with

Table 2: Summary of simulations performed. The number of entrained and degassed bubbles refers to resolved bubbles measured over $t \in [40, 70]$.

Fr^2	Re	# of Sims	Entrained	Degassed
5	1000	6	380	236
8	1000	6	1401	1010
10	1000	5	2001	1390
15	1000	5	4190	2884
20	1000	3	4226	2611

different realizations of the initial velocity perturbation to obtain an ensemble data set. Because more bubbles are present at larger Fr^2, fewer ensemble simulations are performed with increasing Fr^2. In total, we perform 25 simulations over $t \in [0, 130]$.

Simulations were performed on 288 cores distributed across 6 nodes of HPE SGI 8600 systems with Intel 8168 Skylake CPUs, located at the U.S. Navy DoD Supercomputing Resource Center (Navy DSRC). Each simulation took 30 hours. In total, the simulations presented in this work used ~200,000 core hours.

ELA Snapshot Interval

For ELA, we need to determine an appropriate snapshot interval T_s. The minimum T_s depends on the numerical accuracy of the CCL method, and the maximum T_s is set by the largest $\lambda(a)$ we wish to accurately capture.

On the accuracy of CCL, determining contiguous regions of air is equivalent to reconstructing the interface separating air and water based on the (discrete) VOF field. Because there is not a unique geometric reconstruction, there is ambiguity in whether nearby regions of air are connected or not on discrete grids. Practically, this means that, on short timescales, CCL methods will generate spurious fragmentation/coalescence or entrainment/degassing pairs of events. To avoid these spurious events, Chan *et al.* (2021) recommends $T_s \Omega > 0.1$, where

$$\Omega = 0.42 \varepsilon^{1/3} a^{-2/3} \tag{21}$$

is the fragmentation frequency of a relevant bubble radius a (Martínez-Bazán *et al.*, 1999). Following Gaylo *et al.* (2022), we chose $a = a_{\text{res}}$. For the dissipation rate $\varepsilon \approx 0.0005$ from DNS by Yu *et al.* (2019) (verified *a posteriori*, see Fig. 4) to obtain $T_s > 0.3$.

As discussed above, we may miss the entrainment and degassing of a bubble if the two events are separated by less than T_s. In terms of the degassing rate, this means we can only accurately measure $\lambda(a) \leq 1/T_s$. Because the largest expected value of $\lambda(a)$ is unclear, we performed the simulations with three concurrent instances of ELA with

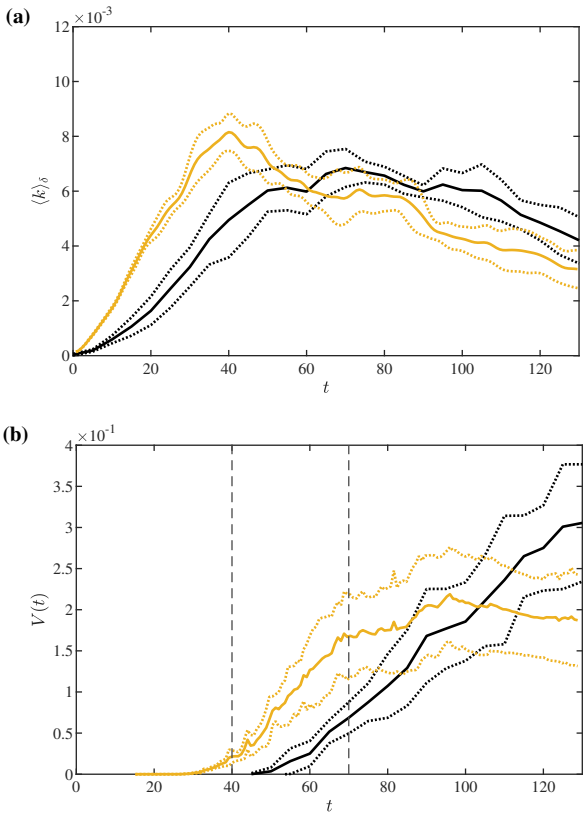

Figure 3: Comparison of the ensemble average (a) turbulent kinetic energy and (b) total volume of entrained air for $Fr^2 = 10$ between (——) our simulations; and (——) reported by Yu *et al.* (2019). The dotted lines in the respective colors indicate one standard deviation and (- - - -) indicate the period of quasi-steady entrainment.

$T_s = [0.4, 0.8, 1.6]$ respectively. *A posteriori*, we chose $T_s = 0.8$ as the largest T_s which reasonably resolves $\lambda(a)$.

TURBULENCE PROPERTIES

In this section we investigate the properties of the turbulence near the free surface. For analysis, we consider turbulence averaged in the water phase,

$$\langle \cdot \rangle_\delta \equiv \frac{\iiint \cdot \, (1 - c) \, \mathrm{d}\mathbf{x}}{\iiint (1 - c) \, \mathrm{d}\mathbf{x}} \quad \text{for } z > -\delta \quad , \tag{22}$$

where $\delta = 0.2$ captures the near-surface region (Yu *et al.*, 2019).

Evolution of Near-Surface Turbulence

For $Fr^2 = 10$, Fig. 3 shows the evolution of the turbulent kinetic energy,

$$\langle k \rangle_\delta = \frac{\langle \mathbf{u}' \cdot \mathbf{u}' \rangle_\delta}{2} \tag{23}$$

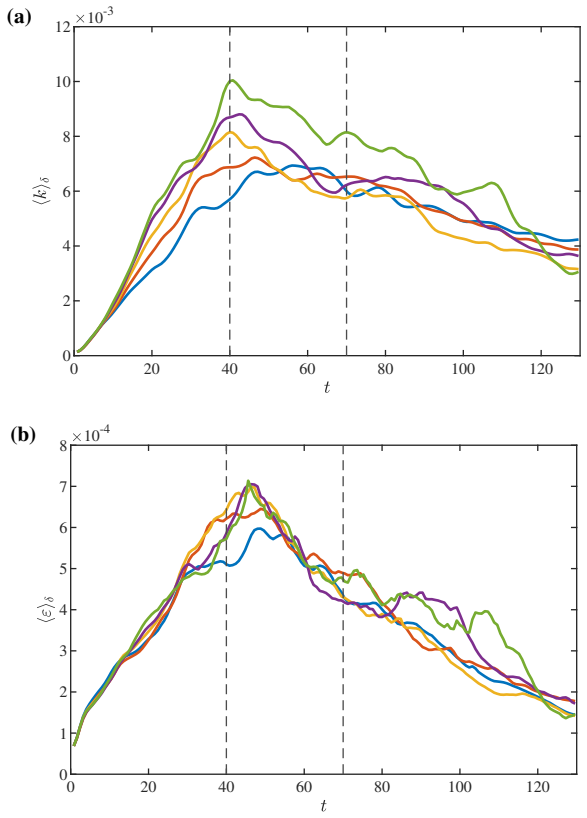

Figure 4: Ensemble average (a) kinetic energy and (b) turbulent dissipation rate in the near-surface for (——) $Fr^2 = 5$; (——) $Fr^2 = 8$; (——) $Fr^2 = 10$; (——) $Fr^2 = 15$; and (——) $Fr^2 = 20$. (- - - -) indicate the period of quasi-steady entrainment.

where $\mathbf{u}' = \mathbf{u} - \langle \mathbf{u} \rangle_\delta$, including a comparison to Yu *et al.* (2019), who also performed an ensemble of 5 simulations at $Fr^2 = 10$. We obtain similar magnitudes, but because we use a stronger initial turbulence intensity to perturbate the shear flow, $\langle k \rangle_\delta$ reaches a maximum earlier and the peak is slightly more pronounced. Related, we see the entrained volume begins to increase earlier. For the range of Fr^2 here, we find that over $t \in [40, 70]$, $\langle k \rangle_\delta$ and the rate of change of total entrained volume $\partial V / \partial t$ regains relatively constant (see Fig. 4a and Fig. 3b respectively). We define $t \in [40, 70]$ here as the quasi-steady entrainment period and will focus on this period.

Turbulent Froude Number

While the shear Froude number Eq. (19) is prescribed by the simulation setup, it uses the characteristic scales of the shear flow. This makes it difficult to use when comparing to other canonical FST problems, such as forced FST (Guo & Shen, 2009). As our research interest is FST generally, it is preferable to consider the characteristic scales of the near-surface turbulence rather than the shear flow.

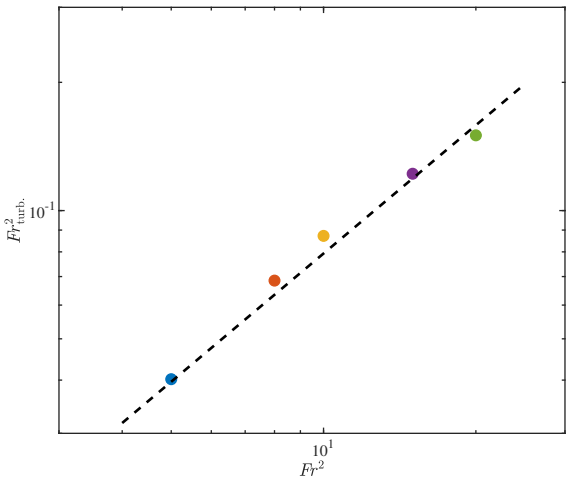

Figure 5: Relationship between the shear-flow Froude number Fr^2 and the turbulence Froude number $Fr^2_{\text{turb.}}$ over $t \in [40, 70]$, including (- - - -) the linear fit given by Eq. (26) with $C = 0.0079$.

To characterize the turbulence, we use the velocity $u_{\text{rms}} = \sqrt{2k/3}$. Yu *et al.* (2019) showed that the turbulence in the near-surface region is isotropic and follows the Kolmogorov spectrum for entraining FST, so the characteristic length scale is

$$L_{\text{turb.}} = \frac{u^3_{\text{rms}}}{\varepsilon} \quad , \tag{24}$$

where ε is the turbulent dissipation rate. Using these velocity and length scales measured in the near-surface region, we define the turbulent Froude number for FST,

$$Fr^2_{\text{turb.}} \equiv \frac{\langle \varepsilon \rangle_\delta}{g\sqrt{2\langle k \rangle_\delta / 3}} \tag{25}$$

Fig. 4 shows our ensemble measurements of $\langle \varepsilon \rangle_\delta$ and $\langle k \rangle_\delta$ across $Fr^2 \in [5, 20]$. We see that $\langle \varepsilon \rangle_\delta$ is independent of Fr^2 and $\langle k \rangle_\delta$ depends only weakly on Fr^2. This means that the relationship between the shear flow Froude number Fr^2 and $Fr^2_{\text{turb.}}$ should be linear

$$Fr^2_{\text{turb.}} \approx C\, Fr^2 \quad . \tag{26}$$

Fig. 5 confirms this relationship, and least-squares regression gives $C = 0.0079$.

ENTRAINMENT AND DEGASSING STATISTICS

In this section we investigate the statistics of entrainment and degassing, obtained using ELA. Unless otherwise noted, these statistics come from the period of quasi-steady

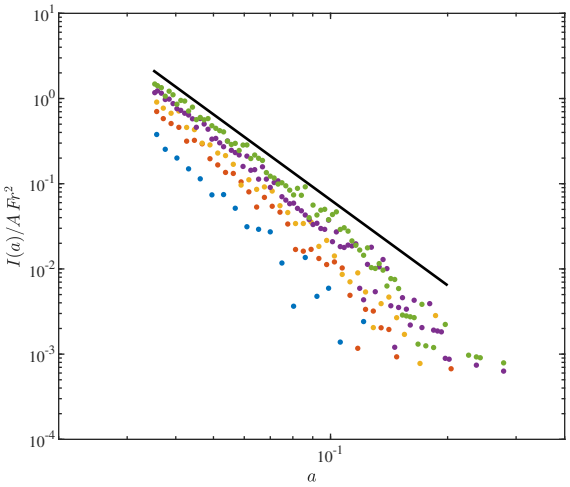

Figure 6: Entrainment size distribution for (•) $Fr^2 = 5$; (•) $Fr^2 = 8$; (•) $Fr^2 = 10$; (•) $Fr^2 = 15$; and (•) $Fr^2 = 20$. (——) shows $\propto a^{-10/3}$ predicted by Yu *et al.* (2020).

entrainment $t \in [40, 70]$ and represent the ensemble average of simulations at a given Fr^2. Size distributions will only include resolved bubbles radius $a > a_{\text{res}}$.

Entrainment Size Distribution, $I(a)$

We start with the entrainment size distribution, $I(a)$. Because entrainment represents the transport of air across the free surface into the water, we normalize $I(a)$ by the surface area of the undisturbed free surface, $A = (10.472)^2$.Yu *et al.* (2020) consider an entrainment size distribution based on total entrainment over the entire quasi-steady entrainment period (units $[1/L]$), rather than the entrainment per unit time ($I(a) := [1/LT]$) we consider. Still, their mechanistic argument for the scaling of entrainment with bubble radius is applicable to $I(a)$.

Fig. 6 shows the entrainment size distribution measured using ELA. As predicted by Yu *et al.* (2020), we observe $I(a) \propto a^{-10/3}$. We highlight that this is the first time this size distribution has been directly measured, as opposed to inferred from the bubble population distribution $N(a)$. In the next section we show degassing is significant in air entraining FST. And this, along with how quickly fragmentation cascades change $N(a)$ (Gaylo *et al.*, 2023), show that $I(a)$ cannot generally be inferred from measurements of $N(a)$.

Relative Volume Flow Rates, Q_D/Q_I

We now examine the volume flow rate of air during FST entrainment. Recall Eq. (5): the change in total entrained volume, $\partial V/\partial t$, is the difference between the flow of air from the sky to bubbles by entrainment, Q_I, and the flow of air from bubbles to the sky by degassing Q_D. Again, it is useful to normalize these values by A, the surface area of the undisturbed free surface.

Previous work only had access to the net effect of entrainment and degassing, $\partial V/\partial t$. For $Fr^2 = 10$, Fig. 7 shows $\partial V/\partial t$, the derivative of $V(t)$ shown in Fig. 3b. Derivatives amplify statistical noise, so it is useful to introduce a low-pass filter to facilitate qualitative analysis. We use a simple moving average

$$\widetilde{f}(t) \equiv \frac{1}{W}\int_{-W/2}^{W/2} f(t+t')\,\mathrm{d}t' \quad , \tag{27}$$

where the window $W = 16$ (corresponding to $20\,T_s$) was chosen as a balance between noise reduction and temporal resolution. Apart from changes in the level of apparent statistical noise, the qualitative trends do not change with W. $V(t)$ increases steadily over the quasi-steady entrainment period $t \in [40, 70]$, so as expected $\partial V/\partial t > 0$ over the same period in Fig. 7.

Using ELA, we can now obtain Q_I and Q_D, the contributions to $\partial V/\partial t$, separately. For $Fr^2 = 10$, these results (as measured every T_s and smoothed by Eq. (27)) are shown in Fig. 8. $\partial V/\partial t > 0$ over the quasi-steady entrainment period so $Q_I > Q_D$ must be true. Still, we find that the magnitude of Q_D is close to Q_I, showing that degassing is significant in entraining FST and has a large effect on the total entrained volume of air.

To evaluate the effect of Fr^2 on the relative strength of degassing, Q_D/Q_I, we repeat the analysis shown in Fig. 8 for each Fr^2. A sensitivity analysis (not shown) confirms that Q_D/Q_I does not depend on the choice of T_s. Fig. 9 shows that degassing is always significant during the quasi-steady entrainment period, i.e., $Q_D/Q_I \sim O(1)$. Additionally, the relative strength of degassing is independent of Fr^2.

Degassing Rate, $\lambda(a)$

Having shown that degassing is significant during FST entrainment, we now investigate its size distribution. Fig. 10 shows the degassing spectrum $D(a)$. As expected based on Q_D/Q_I, the magnitude of the degassing spectrum is smaller but still of the same order-of-magnitude as the entrainment spectrum $I(a)$.

As discussed earlier, it is useful to describe degassing in terms of the degassing rate $\lambda(a)$, shown in Fig. 11. For the largest bubbles, we see some effect of the $1/T_s$ upper limit on measurable $\lambda(a)$; however, for the majority of bubble sizes, $\lambda(a)$ is well resolved. Note that statistical noise increases with radius due to smaller sample sizes. Larger bubbles are rarer, hence degassing of larger bubbles is rarer (see Fig. 10).

We see that $\lambda(a)$ increases with bubble radius, i.e., smaller bubbles remain entrained longer than larger bubbles. This is consistent with observations in the far wake (Trevorrow *et al.*, 1994) and implies that bubble rise velocity is relevant to degassing rates. To elucidate the scaling of $\lambda(a)$, we start by analyzing which bubble-rise

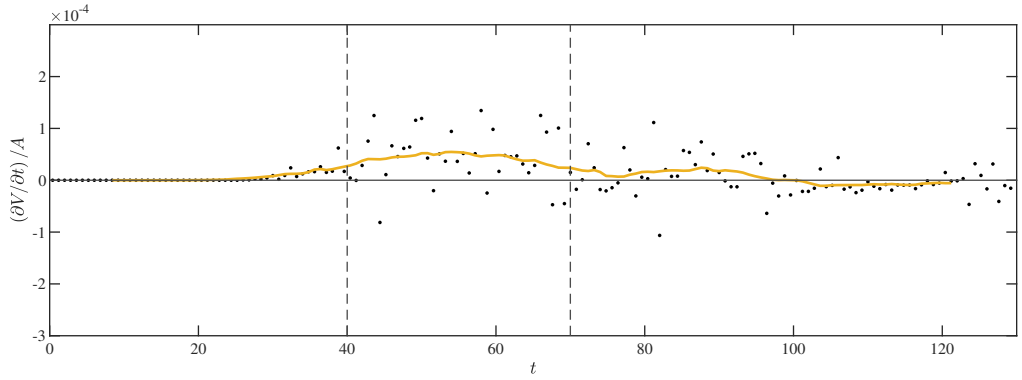

Figure 7: Rate of change of entrained volume $\partial V/\partial t$ for $Fr^2 = 10$ (•) as measured and (——) smoothed. (- - - -) indicate the period of quasi-steady entrainment.

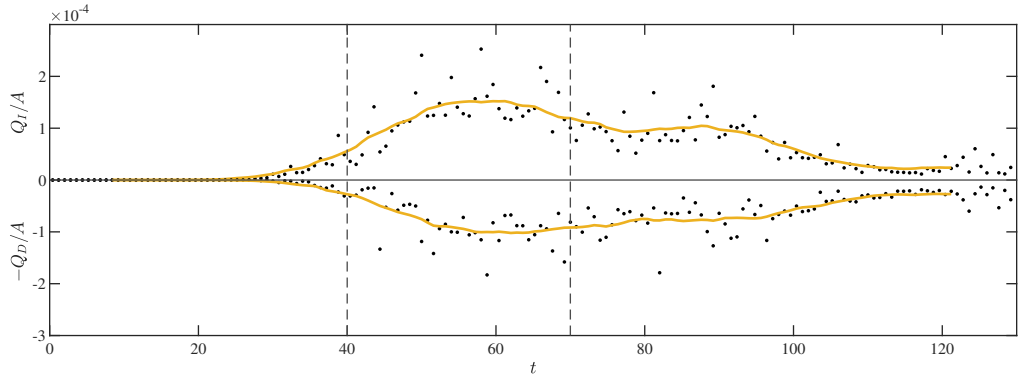

Figure 8: On the positive y-axis, entrainment flow rate Q_I for $Fr^2 = 10$ (•) as measured and (——) smoothed. On the negative y-axis, degassing flow rate Q_D for $Fr^2 = 10$ (•) as measured and (——) smoothed. (- - - -) indicate the period of quasi-steady entrainment.

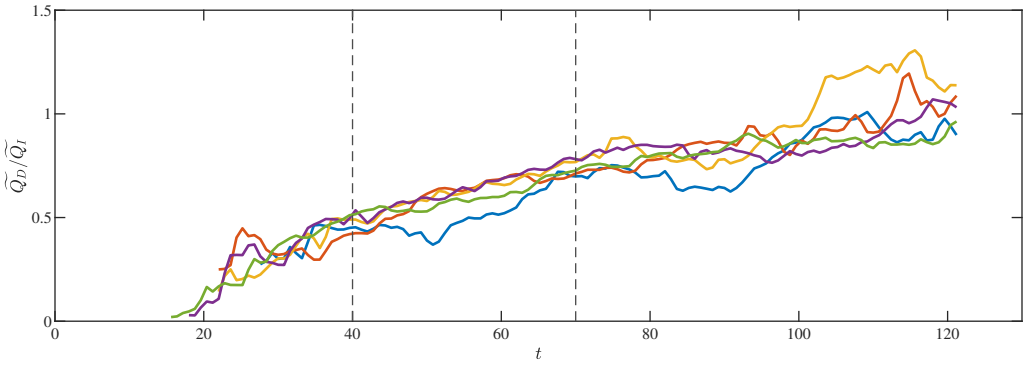

Figure 9: Relative strength of degassing for (——) $Fr^2 = 5$; (——) $Fr^2 = 8$; (——) $Fr^2 = 10$; (——) $Fr^2 = 15$; and (——) $Fr^2 = 20$. (- - - -) indicate the period of quasi-steady entrainment.

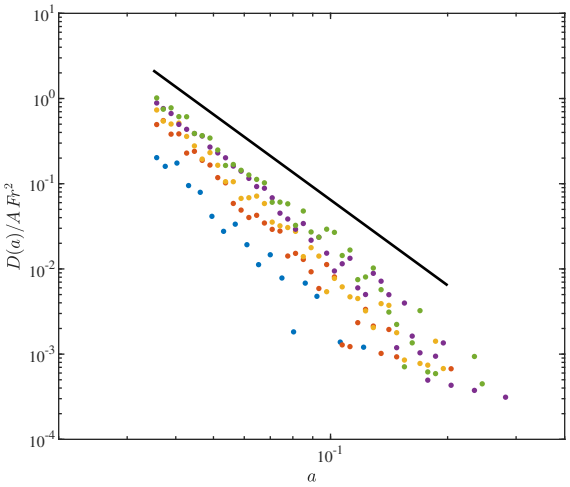

Figure 10: Degassing size distribution for (•) $Fr^2 = 5$; (•) $Fr^2 = 8$; (•) $Fr^2 = 10$; (•) $Fr^2 = 15$; and (•) $Fr^2 = 20$. For reference, (——) is the same as in Fig. 6.

regime is present. Assuming the inertial regime, table 1 (Park *et al.*, 2017) gives the bubble-rise Reynolds,

$$Re_{b,\text{Inertial}} = 0.816\ \text{g}^{5/6}\nu^{-5/3}a^{5/2} \quad , \tag{28}$$

which is valid if $1 < Re_{b,\text{Inertial}} < 100$. For $Re = 1000$ here, the bounds are

$$0.0108\ (Fr^2)^{1/3} < a < 1.08\ (Fr^2)^{1/3} \tag{29}$$

For the largest $Fr^2 = 20$, the lower bound is 0.02 and for the smallest $Fr^2 = 5$ the upper bound is 1.8, meaning all reported bubbles are in the inertial regime where the vertical rise velocity is

$$W_t(a) = 0.408\ \text{g}^{5/6}\nu^{-2/3}a^{3/2} \tag{30}$$

While we expect rise velocity to be important, there is also strong turbulence in the near-surface region which advects bubbles, introducing an additional characteristic velocity, u_{rms}. For $u_{\text{rms}} \gg W_t$ (small bubbles), we expect turbulence to be significant to the rise and subsequent degassing of bubbles. For $u_{\text{rms}} \ll W_t$ (large bubbles), we expect bubbles to rise as in quiescent flow. This implies a transition at $u_{\text{rms}} = W_t$, corresponding to a critical radius

$$a_c = 1.82\ {u_{\text{rms}}}^{2/3}\,\nu^{4/9}\,\text{g}^{-5/9} \quad . \tag{31}$$

When we scale bubble radius by a_c (Fig. 11b), we see a collapse of $\lambda(a)$ and a transition at $a/a_c \sim O(1)$. This collapse demonstrates the relevance of W_t and u_{rms} to the two observed regimes of degassing.

One might hypothesize that $\lambda(a)$ should scale like the relevant characteristic velocity, u_{rms} for $a \ll a_c$ and

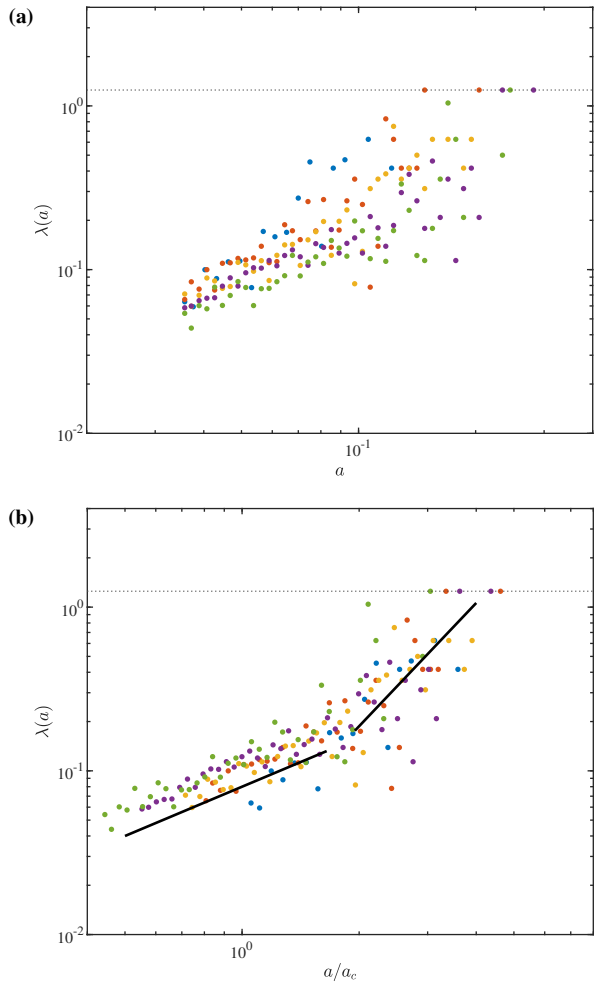

Figure 11: Degassing rate as a function of (a) bubble radius a and (b) scaled bubbles radius a/a_c for (•) $Fr^2 = 5$; (•) $Fr^2 = 8$; (•) $Fr^2 = 10$; (•) $Fr^2 = 15$; and (•) $Fr^2 = 20$. (——) illustrates $\lambda \propto a$ and $\lambda \propto a^{5/2}$. (· · · · · ·) indicates $1/T_s$.

$W_t(a)$ for $a \gg a_c$. This would imply $\lambda(a \ll a_c) \propto$ const. and $\lambda(a \gg a_c) \propto a^{3/2}$. However, Fig. 11b shows that the observed scaling seems to be larger for each regime by a factor of a: $\lambda(a \ll a_c) \propto a$ and $\lambda(a \gg a_c) \propto a^{5/2}$. We note that comparing λ (units $[1/T]$) to a velocity (units $[L/T]$) still leaves a characteristic length scale. A full mechanistic explanation for the scaling of $\lambda(a)$ is an area of ongoing work.

CONCLUSION

Air-entraining free surface turbulence (FST) is relevant to the near wake of the bubbly flow created by a vessel and accurate models for the bubble population created in the near wake are necessary for predicting the extent and characteristics of the whole bubbly wake. This paper

performs ensemble DNS of a canonical shear-flow FST at large Fr^2 sufficient to entrain air. In addition to performing more ensembles than previous work on this flow (Yu *et al.*, 2019; Yu *et al.*, 2020), Eulerian label advection (ELA) (Gaylo *et al.*, 2023), a new numerical bubble tracking tool, allows us to identify entrainment and degassing events and extract their statistics. This first direct measurement of entrainment and degassing provides new insight into these mechanisms, which could not be obtained from only measuring the resulting bubble populations.

Based on turbulent kinetic energy and confirmed by the growth of V, we identify the period of quasi-steady entrainment for our (unsteady) shear-flow FST. During this period, we measure the turbulence in the near-surface region to provide a Froude number based on the characteristic scales of isotropic turbulence rather than characteristics of the shear profile. This will allow comparison of our shear-flow FST to other FST flows.

For the quasi-steady entrainment period, we obtain the first direct measurement of the entrainment size distribution. We observe the $I(a) \propto a^{-10/3}$ power law predicted by Yu *et al.* (2020) using the balance between locally available turbulent kinetic energy and bubble potential energy.

With the ability to directly measure entrainment and degassing as opposed to only their net effect on the total entrained volume V, we evaluate the relative strength of degassing compared to entrainment, as measured by the ratio of degassing volume flow rate Q_D to entrainment volume flow rate Q_I. When the total entrained volume is increasing ($\partial V/\partial t > 0$) we know degassing is weaker than entrainment ($Q_D \leq Q_I$). However, we show that degassing is still significant for air-entraining FST. For all Fr^2, we observe $Q_D/Q_I \sim O(1)$. These results show that models for degassing included to make accurate predictions of the volume of entrained air in the near wake.

Knowing that degassing plays a significant role in determining the bubble population in air-entraining FST, we examine the size distribution of degassing. Assuming that degassing is an independent process for each bubble, we focus on the degassing rate $\lambda(a)$, defined as the ratio of the degassing size distribution $D(a)$ to the bubble population size distribution $N(a)$. We find large bubbles have a faster degassing rate, consistent with observations relevant to the far wake, where degassing depends on bubble rise velocity $W_t(a)$. For the near wake, we expect turbulent advection to also be relevant, leading to a critical radius a_c where $u_{\text{rms}} = W_t(a_c)$. We find that a_c predicts the transition between two observed regimes of $\lambda(a)$. We report the observed scaling of $\lambda(a)$ in each regime, and development of a mechanistic explanation is ongoing work.

ACKNOWLEDGMENTS

This work was funded by the U.S. Office of Naval Research grant N00014-20-1-2059 under the guidance of Dr. W.-M. Lin. This work was supported in part by high-performance computer time and resources from the DoD High Performance Computing Modernization Program.

REFERENCES

Castro, A.M. and Carrica, P.M., "Bubble size distribution prediction for large-scale ship flows: Model evaluation and numerical issues," Int. J. Multiphase Flow, 12 2013, Vol. 57, pp. 131–150.

Castro, A.M., Li, J., and Carrica, P.M., "A mechanistic model of bubble entrainment in turbulent free surface flows," Int. J. Multiphase Flow, 2016, Vol. 86, pp. 35–55.

Chan, W.H.R., Dodd, M.S., Johnson, P.L., and Moin, P., "Identifying and tracking bubbles and drops in simulations: A toolbox for obtaining sizes, lineages, and breakup and coalescence statistics," J. Comput. Phys., 5 2021, Vol. 432, p. 110156.

Deane, G.B. and Stokes, M.D., "Scale dependence of bubble creation mechanisms in breaking waves," Nature, 2002, Vol. 418, pp. 839–844.

Dimas, A.A. and Triantafyllou, G.S., "Nonlinear interaction of shear flow with a free surface," J. Fluid Mech., 2 1994, Vol. 260, pp. 211–246.

Falgout, R., Jones, J., and Yang, U., "The Design and Implementation of *hypre*, a Library of Parallel High Performance Preconditioners," A. Bruaset and A. Tveito, (eds.) Numerical Solution of Partial Differential Equations on Parallel Computers, Vol. 51, Springer-Verlag, 2006, pp. 267–294.

Garrett, C., Li, M., and Farmer, D., "The Connection between Bubble Size Spectra and Energy Dissipation Rates in the Upper Ocean," J. Phys. Oceanogr., 2000, Vol. 30, No. 9, pp. 2163–2171.

Gaylo, D.B., Hendrickson, K., and Yue, D.K., "Effects of power-law entrainment on bubble fragmentation cascades," J. Fluid Mech., Jun. 2021, Vol. 917, No. 9, p. R1.

Gaylo, D.B., Hendrickson, K., and Yue, D.K., "An Eulerian label advection method for conservative volume-based tracking of bubbles/droplets," J. Comput. Phys., Aug. 2022, Vol. 470, p. 111560.

Gaylo, D.B., Hendrickson, K., and Yue, D.K., "Fundamental time scales of bubble fragmentation in homogeneous isotropic turbulence," J. Fluid Mech., 5 2023, Vol. 962, p. A25.

Guo, X. and Shen, L., "On the generation and maintenance of waves and turbulence in simulations of free-surface turbulence," J. Comput. Phys., 10 2009, Vol. 228, pp. 7313–7332.

He, L., Ren, X., Gao, Q., Zhao, X., Yao, B., and Chao, Y., "The connected-component labeling problem: A review of state-of-the-art algorithms," Pattern Recognit., 2017, Vol. 70, pp. 25–43.

Hendrickson, K., Weymouth, G.D., Yu, X., and Yue, D.K.P., "Wake behind a three-dimensional dry transom stern. Part 1. Flow structure and large-scale air entrainment," J. Fluid Mech., 2019, Vol. 875, pp. 854–883.

Hendrickson, K., Weymouth, G.D., and Yue, D.K., "Informed component label algorithm for robust identification of connected components with volume-of-fluid method," Comput. Fluids, 2020, Vol. 197, p. 104373.

Hinze, J.O., "Fundamentals of the hydrodynamic mechanism of splitting in dispersion processes," AIChE J., 1955, Vol. 1, pp. 289–295.

Klein, M., Sadiki, A., and Janicka, J., "A digital filter based generation of inflow data for spatially developing direct numerical or large eddy simulations," J. Comput. Phys., 4 2003, Vol. 186, pp. 652–665.

Martínez-Bazán, C., Montañés, J.L., and Lasheras, J.C., "On the breakup of an air bubble injected into a fully developed turbulent flow. Part 1. Breakup frequency," J. Fluid Mech., 1999, Vol. 401, pp. 157–182.

Mattingly, G.E. and Criminale, W.O., "The stability of an incompressible two-dimensional wake," J. Fluid Mech., 1972, Vol. 51, pp. 233–272.

NDRC, "Acoustic properties of wakes," Physics of Sound in the Sea, Vol. 8, Office of Scientific Research and Development, Washington, D. C., 1946, pp. 441–559.

Park, S.H., Park, C., Lee, J., and Lee, B., "A Simple Parameterization for the Rising Velocity of Bubbles in a Liquid Pool," Nucl. Eng. Technol., 6 2017, Vol. 49, pp. 692–699.

Ruth, D.J., Vernet, M., Perrard, S., and Deike, L., "The effect of nonlinear drag on the rise velocity of bubbles in turbulence," J. Fluid Mech., 10 2021, Vol. 924, p. A2.

Thorpe, S.A., "On the clouds of bubbles formed by breaking wind-waves in deep water, and their role in air-sea gas transfer," Philos. Trans. Royal Soc. A, 2 1982, Vol. 304, pp. 155–210.

Trevorrow, M.V., Vagle, S., and Farmer, D.M., "Acoustical measurements of microbubbles within ship wakes," J. Acoust. Soc, Apr. 1994, Vol. 95, No. 4, pp. 1922–1930.

Weymouth, G. and Yue, D.K., "Conservative Volume-of-Fluid method for free-surface simulations on Cartesian-grids," J. Comput. Phys., Apr. 2010, Vol. 229, No. 8, pp. 2853–2865.

Yu, X., Hendrickson, K., Campbell, B.K., and Yue, D.K., "Numerical investigation of shear-flow free-surface turbulence and air entrainment at large Froude and Weber numbers," J. Fluid Mech., 2019, Vol. 880, pp. 209–238.

Yu, X., Hendrickson, K., and Yue, D.K., "Scale separation and dependence of entrainment bubble-size distribution in free-surface turbulence," J. Fluid Mech., 2020, Vol. 885, p. R2.

DISCUSSION

P. M. Carrica, General Dynamics Electric Boat.

This paper presents DNS of bubble entrainment in a shear flow. A significant contribution of the paper is the quantification of bubble degassing through tracking of individual bubbles. As is usually the case with this team the work is excellent and very well presented. I have a couple of points to spur discussion:

1. DNS appears to be used loosely in the paper. A true DNS would require proper resolution of

   (a) The Kolmogorov scale to capture the TKE dissipation adequately.

   (b) The flow around the bubbles that determine the drag, deformation, curvature, surface tension forces, etc.

   (c) The pinch-off and shear that dominate bubble breakup (mostly of the smallest bubbles) and the fluid film drainage that dominates bubble coalescence.

   Can you quantify to what extent these parameters are satisfied for your simulations? I expect that resolution is adequate for the larger bubbles and very poor for smaller bubbles and prediction of coalescence, since the resolutions required to resolve those phenomena are extreme. Can you discuss to the best of your knowledge and experience how under resolution could affect results?

2. The fact that direct tracking of bubbles is used is a game changer in the study of entrainment and degassing. This paper shows a variety of interesting trends but for the sake of time I'll focus only on Fig. 11a. The general trend of larger bubbles degassing faster is expected, but what is the distribution of $\lambda(a)$ for various a? Is it Gaussian? Does the standard deviation correlate with the local turbulence? These kind of parameters would aid modeling of degassing to improve entrainment models.

AUTHOR'S REPLY

We thank Professor Carrica for his questions, addressed below.

Question 1

Starting with the TKE dissipation, for the Kolmogorov scale we use $\eta = (\nu^3/\varepsilon)^{1/4}$. Figure 4 shows ε near the free surface, where we expect the strongest turbulence (largest ε). After scaling (recall $Re = 1000$), $\varepsilon \approx 6 \times 10^{-4}$ gives $\eta/\Delta x \approx 1.3$. $\eta/\Delta x > 1$ confirms the TKE dissipation is adequately captured.

While proper resolution of turbulence is the typical definition of DNS for single-phase flow, Professor Carrica is correct that two-phase flows have a variety of other physics which must be properly resolved. An important measure for resolving the physics of a bubble is $a/\Delta x$, the number of grid points per its (effective) radius a. We note that, for $We \sim \infty$, it is possible for the flow here to create arbitrarily small bubbles. Therefore, it is not possible to obtain sufficient $a/\Delta x$ for all bubbles. Instead, we specify a minimum a_{res} and exclude all bubbles smaller than this from the results. From our experience, $a_{\text{res}} = 1.5\Delta x$ is sufficient to resolve bubble fragmentation in the absence of surface tension. To confirm the entrainment distribution $I(a)$ and degassing rate $\lambda(a)$ are accurately captured for $a > a_{\text{res}}$, we have performed a convergence test. For $Fr^2 = 15$, we perform three runs using a finer $576^2 \times 384$ grid. Figure 12 shows that the measured $I(a)$ and $\lambda(a)$ are independent of grid resolution, meaning our grid captures the relevant physics, including drag as it effects degassing rates. We note that this convergence test is in addition to the convergence test by Yu *et al.* (2019), who also found $384^2 \times 256$ was adequate.

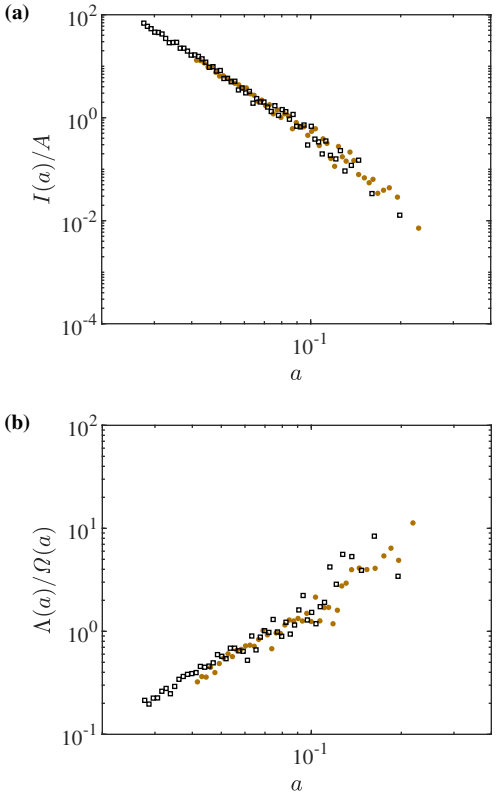

Figure 12: Convergence of entrainment size distribution (a), degassing rate (b) during $t \in [40, 70]$ for $Fr^2 = 15$ with ●, $384^2 \times 256$ and □, $576^2 \times 384$.

Finally, we note that our numerical method does not resolve the thin film drainage associated with coalescence at these resolutions. cVOF can only capture one air-water interface per grid cell (Weymouth & Yue,

2010), which means any bubbles with interfaces within one grid cell will coalesce. This leads to a systematic over prediction of the rate of coalescence. Using ELA to quantify coalescence in our simulations (which have relatively low total void fraction), we find less than 10% of resolved bubbles are involved in a coalescence event during their lifetimes. This suggests that, even with an over-predicted coalescence rate, coalescence has only a minor effect on our reported bubble population.

Question 2

While possible to investigate the correlation between local turbulence and degassing, the simulations presented here did not record enough information to obtain the necessary instantaneous spatial distributions of $\lambda(a)$. We agree this would be interesting to investigate in the future, but note that many more ensemble simulations would be needed to obtain statistical convergence of such correlations.

For the statistical distribution of degassing rate $\lambda(a)$ at various a, we consider the distribution of the life time of bubbles between entertainment and degassing, T_b. For bubbles that were entrained and then degassed without any other processes (e.g., fragmentation) happening in between, the degassing rate $\lambda(a)$ can be related to this distribution by $E[T_b] = 1/\lambda(a)$. As a representative example, figure 13 shows the measured probability distribution function of T_b, $f_{T_b}(t_b)$, for bubbles of radius $a \in [0.08, 0.1]$ from the $Fr^2 = 15$ simulations. Many bubbles degass after very short t_b, but after that the distribution of t_b appears to be roughly exponential,

$$f_{T_b}(t_b) = C \exp[-Ct_b] \quad , \tag{32}$$

not Gaussian. Physically, one would expect a Gaussian distribution if bubbles followed roughly similar parabolic paths, leading to clustering of t_b around the mean. Instead, the exponential PDF implies that degassing can be treated as a Poisson process where the history of a bubble has little effect on the probability of degassing. From a modeling perspective, this memory-less nature of Poisson processes could be convenient.

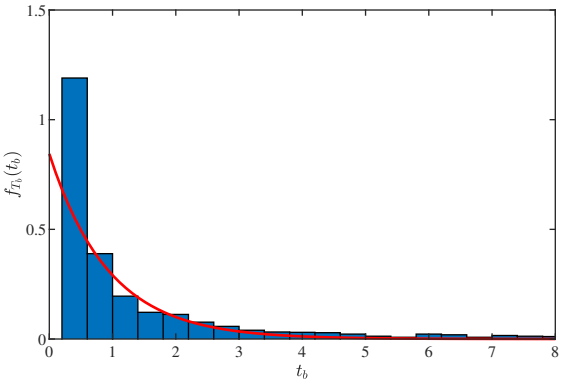

Figure 13: Probability distribution function $f_{T_b}(t_b)$ of time between entrainment and degassing for bubbles of effective radius $a \in [0.08, 0.1]$ for $Fr^2 = 15$. (——) shows the fit (excluding the smallest t_b bin) to an exponential distribution Eq. (32).